Synthetic Aperture Imaging of Multiple Point Targets in Rician Fading Media[*]

Albert C. Fannjiang[†], Knut Solna[‡], and Pengchong Yan[†]

Abstract. This paper presents a study of stability, resolution, and detection for broad-band synthetic aperture (SA) imaging in Rician fading media. The stability condition $BNK^2/(K+1) \gg M$ is derived, where K is the Rician factor, B is the effective number of coherence bands, N is the effective number of array elements, and M is the number of (widely separated) targets. The imaging method is tested numerically with randomly distributed discrete scatterers, and comparisons with the imaging with the full response matrix (RM) are made. The resolution study reveals several interesting effects: First, given the same measurement resources, SA imaging has better resolution performance, although less stable, than RM imaging; second, for both imaging methods, the cross-range resolution measure (i.e., "full width at half maximum") decreases with the aperture (N fixed) and the probe spacing (the total aperture fixed) while the range resolution increases with both parameters. A statistical scheme is introduced to reduce the uncertainty when the stability regime is not realized.

1. Introduction. We investigate synthetic aperture (SA) imaging in a cluttered environment in this paper. An important feature of the propagation channel considered here is that the mean or coherent signals do not vanish. This is the case for what is called, in the wireless literature, a *Rician fading channel*, where, in addition to incoherent signals, there is a significant, nonfluctuating multipath component [16]. Typically a Rician channel arises when line-of-sight or dominant reflectors are present in the medium.

The measurement configuration that we consider is motivated by SA radars. SA imaging is a technique where a substantial aperture can be synthesized by moving a transmit-receive antenna along a trajectory and repeatedly interrogating a search area by firing repeated pulses from the antenna and measuring the responses; see Figure 1. This can greatly leverage a limited probe resource and has many applications in remote sensing. The image formation is obtained via a matched filter technique and typically analyzed in the Born approximation [2]. In SA imaging high resolution is obtained via a chirped pulse combined with a deramping step. This important imaging technique, however, requires an accurate knowledge of the medium [24].
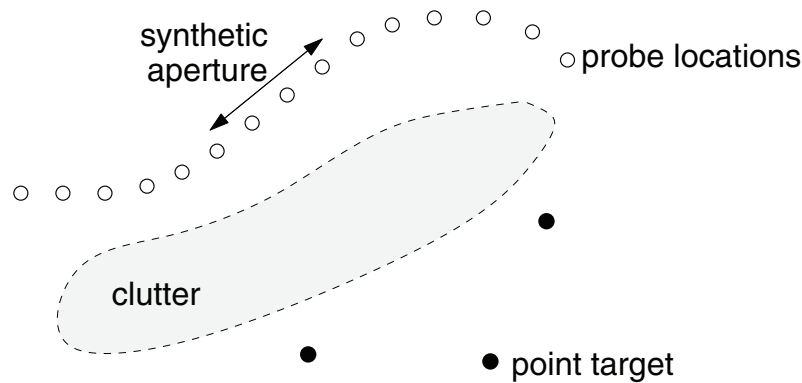
Figure 1. *SA imaging geometry.*

In the present work we consider a simplified configuration with sampling at a set of well-separated frequencies and a set of *fixed* probe locations along the measurement path, therefore neglecting the Doppler effect associated with the relative motion between the antenna and targets. This static set-up is also suitable in applications where the medium is time independent and the relative motion is slow. Our first main interest is then in the stability condition of the image formed from these measurements, that is, to what extent the image and the appearance of targets in it will depend sensitively on the particular clutter realization that happens to be in the scenery. This stability analysis is a continuation of the work in [10], which addresses the stability of imaging with a real, not synthetic, aperture (more on this below).

Let M be the number of sufficiently separated (point) targets, B the number of sufficiently separated frequencies, and N the number of sufficiently separated sample positions of the antenna during the interrogation process. The meaning of "sufficient separation" will be explained in section 2. Our set-up, however, is not restricted to an antenna path of any particular geometry; in principle they can be straight, circular, or arbitrary (Figure 1).

Let K be the Rician factor which is the ratio of the coherent power to the fluctuating (incoherent) power. We show (in section 2 and Appendix A) that for a Rician fading channel a sufficient condition for imaging stability is

$$(1.1) \qquad \frac{K^2 BN}{K+1} \gg M.$$

In contrast, let us consider the following imaging geometry with a real, nonsynthetic aperture: there is exactly one transmit-receive antenna at each of the N sampling positions. For each probe wave all N antennas receive the responses. For each frequency, the impulse responses form a matrix called the response matrix (RM) or the multistatic data matrix. In comparison, SA imaging, as simplified here, uses only the diagonal elements of the RMs. The performance of RM imaging has been analyzed previously [10] and was shown to be stable if

$$(1.2) \qquad KBN \gg M.$$

Condition (1.1) reduces to (1.2) when $K \gg 1$; i.e., the medium is nearly deterministic. On the other hand, when $K \ll 1$, (1.1) becomes $K^2 BN \gg M$, which is significantly worse than

(1.2). In the middle range $K \approx 1$, (1.1) is more severe than (1.2) by a factor of two. The difference in the stability performance between SA and RM imaging will be apparent in our numerical simulations (Figure 4).

The mean-zero case ($K = 0$) of the Rayleigh fading channels occurs in the diffuse regime, which is beyond the scope of the present work. However, it is noteworthy that the above stability condition bears a certain resemblance to the stability condition for time reversal *communications* through the Rayleigh fading channels analyzed in [5] and [6].

Several striking results come from the resolution study for SA and RM imaging (section 4). Our analysis reveals, and the numerics confirm, the following effects: (i) With N, B fixed SA imaging, although less stable, has better resolution performance than RM imaging. The improvement factor is about $\sqrt{2}$ in the transverse resolution and is close to unity in the longitudinal resolution. (ii) For both imaging methods, the cross-range resolution decreases with the aperture (with N fixed) and the antenna/probe spacing (with the total aperture fixed) while the range resolution increases with both parameters (Figures 5, 6, and 7). We use the Houston criterion and define the transverse and longitudinal resolutions to be "full width at half maximum" (FWHM) in the respective directions.

The counterintuitive effect (i) may be attributed to two facts: One is that the differential response matrix is symmetric, and hence redundancy exists in the data. The other is that there is higher degree of correlation among the data in the same row or column than there is along the diagonal because the data in the same row or column come from either the same emitter or the same receiver. Indeed, from this perspective, the diagonal entries are the physically least codependent set of N data in the response matrix. However, as a result of employing less data than RM imaging, the SA image tends to be weaker in intensity (Figure 3) and therefore more susceptible to measurement noise, which is not considered here, in addition to the clutter noise discussed above.

When the stability condition (1.1) is not satisfied, the image becomes noisy. A natural approach to dealing with noise or uncertainty is by statistical detection. In section 5 we develop a detection scheme to improve the imaging performance, which becomes significantly better after the application of the detection scheme. In the case of additive noise, such schemes have been shown to improve resolution performance beyond the classical Rayleigh resolution limit in the case of a high signal-to-noise ratio [3, 9, 12, 17, 20, 21, 23]. Here under the Rician fading assumption and other approximations, we apply the scheme to handle the multiplicative clutter noise. The scheme can be extended to RM imaging when (1.2) is violated, but we do not pursue this here.

2. SA and RM imaging. Let $H(\mathbf{x}, \mathbf{y}; \omega)$ be the transfer function of the propagation channel at the frequency ω from point $\mathbf{y}$ to $\mathbf{x}$. If the propagation channel is described by a randomly fluctuating refractive index $n^2(\mathbf{x})$, then H is the Green function of the Helmholtz equation, i.e.,

$$\Delta H(\mathbf{x}, \mathbf{y}; \omega) + k^2 n^2(\mathbf{x}) H(\mathbf{x}, \mathbf{y}; \omega) = \delta(\mathbf{x} - \mathbf{y}),$$

where $k = \omega/c$ is the wavenumber. Hereafter we shall assume the background phase velocity $c = 1$. In our numerical simulation, we use randomly distributed point scatterers whose Green function is determined by the Foldy–Lax equation (section 3).

Denote $H_{mn}(\omega) = H(\mathbf{x}_m, \mathbf{y}_n; \omega)$. Let $\mathbf{H}(\omega) = [H_{mn}(\omega)]$ be the transfer matrix between

the antennas located at $\mathbf{y}_n$, $1 \leq n \leq N$, and targets located at $\mathbf{x}_m$, $1 \leq m \leq M$. Reciprocity implies that $\mathbf{H}(\omega)$ is a symmetric matrix. Moreover, $H_{mn}^*(\omega) = H_{mn}(-\omega)$, where $*$ stands for complex conjugation.

We decompose the random transfer function H into the mean $\bar{H}$ and the fluctuations h, $\mathbb{E}h = 0$, as

$$(2.1) \qquad H(\mathbf{x}, \mathbf{y}; \omega) = \bar{H}(\mathbf{x}, \mathbf{y}; \omega) + h(\mathbf{x}, \mathbf{y}; \omega).$$

The mean and fluctuations are also known as the coherent and diffuse fields, respectively. We write $\bar{\mathbf{H}}(\omega) = [\bar{H}_{mn}(\omega)]$ and $\mathbf{h}(\omega) = [h_{mn}(\omega)]$ with $h_{mn}(\omega) = h(\mathbf{x}_m, \mathbf{y}_n; \omega)$.

Our main assumptions are that (i) the separations of the frequencies ω_l, $l = 1, 2, \ldots, B$, used for imaging are larger than the coherence bandwidth β_c of the channel, and (ii) the spacings of the antennas (or probes) are wider than the coherence length ℓ_c of the channel; see [8, 6] for a more detailed discussion. Moreover, we assume the idealized situation when h is circularly Gaussian with zero mean. As a result of these assumptions we have

$$(2.2) \qquad \mathbb{E}\left[h_{ij}(\omega_k)h_{mn}^*(\omega_l)\right] \approx \eta^2 \delta_{im}\delta_{jn}\delta_{k,l}, \quad \mathbb{E}\left[h_{ij}(\omega_k)h_{mn}(\omega_l)\right] \approx 0 \quad \forall i, j, k, l, m, n,$$

where η^2 is the intensity of fluctuations.

We assume that the multiple targets are point scatterers themselves but the multiple scattering effect involving the targets are negligible (e.g., when they are far apart and/or their scattering strength is weak). This assumption is a form of the so-called *distorted wave Born approximation* (DWBA), except that in the present set-up the background Green function is unknown. In the simulation presented in section 3.1, the scattering strength of the targets is much smaller than that of the clutter so that DWBA is justified. Note, however, that our numerical algorithm is exact and does not use DWBA.

We consider the method of the *differential response*. In this approach, probe waves of various frequencies are first used to survey the random media in the absence of targets. Then in the presence of targets (with unknown locations) the same set of probe waves is used again to survey the media which is assumed to be fixed. The differences between these two responses, called the differential responses, is then used to image the targets.

Let $\tau_i(\omega_l)$ be the reflectivity of target i at frequency ω_l. The differential responses received by the antenna at the location $\mathbf{y}_n$ for targets at locations $\mathbf{x}_i$, $1 \leq i \leq M$, are given by $\sum_{i=1}^{M} \tau_i(\omega_l)H_{in}(\omega_l)H_{in}(\omega_l)$, $l = 1, \ldots, B$. We consider the imaging function

$$(2.3) \qquad u(\mathbf{x}) = \sum_{l=1}^{B}\sum_{j=1}^{N}\sum_{i=1}^{M} \tau_i(\omega_l)H_{ij}^2(\omega_l)P(\mathbf{y}_j, \mathbf{x}; \omega_l)P(\mathbf{x}, \mathbf{y}_j; \omega_l).$$

Note that in the differential field approach, the wave field is back-scattered by the clutter but does not reach the targets and is removed. In comparison, the RM imaging function takes the form

$$(2.4) \qquad u(\mathbf{x}) = \sum_{l=1}^{B}\sum_{j,n=1}^{N}\sum_{i=1}^{M} \tau_i(\omega_l)H_{ij}(\omega_l)H_{in}(\omega_l)P(\mathbf{y}_n, \mathbf{x}; \omega_l)P(\mathbf{x}, \mathbf{y}_j; \omega_l),$$

which utilizes all the entries of the differential RM

$$\sum_{i=1}^{M} \tau_i(\omega_l) H_{ij}(\omega_l) H_{in}(\omega_l) \quad \forall j, n.$$

An important ingredient in (2.3) and (2.4) is the choice of the deterministic back-propagator P. A natural candidate is the phase-conjugated, mean Green function of the cluttered medium (see sections 3.2 and 4.1). However, as shown elsewhere [7], the phase-conjugated, mean Green function generally produces images whose maxima do not correspond to the exact location of the target. Indeed, it tends to underestimate the target range. Two unbiased alternatives are the L^2-normalized phase-conjugated mean Green function as in the conventional matched-field processor [1, 19] or the phase processor [10]. The former requires the knowledge of both (relative) amplitude and phase of the mean Green function, while the latter uses only the phase information.

In the present work, as in [10], we work exclusively with the phase processor; namely, we use the *conjugate phase-factor* of the mean Green function as the back-propagator P. Thus $|P| \equiv 1$. This is essentially the choice that uses the least information (i.e., the phase) about the channel to ensure the bottom-line performance of the imaging method, namely, that the maximum point of $|\mathbb{E}u|$ is exactly the location of the target (see section 4 and [7]).

Let K denote the Rician factor

$$K = \frac{|\bar{H}|^2}{\eta^2}.$$

In Appendix A we show that under condition (1.1) the *inverse* normalized variance of the image u,

$$\mathfrak{R}(\mathbf{x}) = \frac{|\mathbb{E}u(\mathbf{x})|^2}{\mathbb{E}\big(|u|^2(\mathbf{x})\big) - \big|\mathbb{E}\big(u(\mathbf{x})\big)\big|^2},$$

tends to infinity. In other words the imaging function will display the targets without ambiguities, independent of the realization of clutter. The argument is the same as that of [10] modified to account for the SA setting.

In practice, the *real* part of u,

(2.5) $$u_{\mathrm{R}}(\mathbf{x}) = \Re\left\{\sum_{l=1}^{B}\sum_{i=1}^{M}\sum_{j=1}^{N} \tau_i(\omega_l) P(\mathbf{x}, \mathbf{y}_j; \omega_l) H_{ij}^2(\omega_l) P(\mathbf{y}_j, \mathbf{x}; \omega_l)\right\},$$

tends to behave more stably than u since $|u|$ and $|u_{\mathrm{R}}|$ are close to each other at the target locations, while the former is by definition larger than the latter elsewhere. As a consequence, the resolution is also improved by using u_{R}; see Figure 3.

3. Randomly distributed point scatterers. In this section we present first the Foldy–Lax formulation for the point scatterer model used in the simulations [11, 14, 15]. More details about this scheme are given in Appendix B for the reader's convenience. This model gives rise to an exact numerical scheme for computing the Green function of the clutter. We discuss in section 3.2 the mean Green function following the effective medium theory. Then we present numerical results for our imaging scheme using both u and u_{R}.
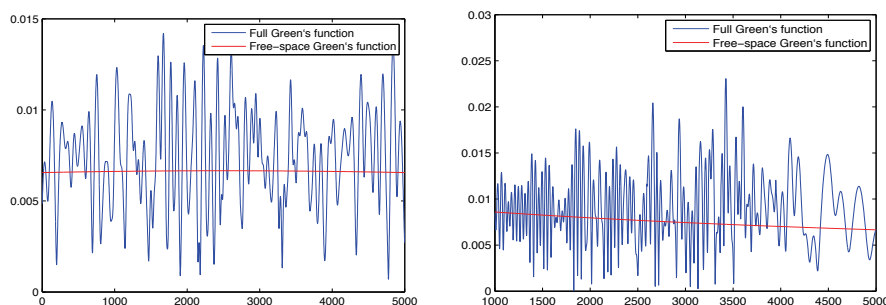
Figure 2. *The transverse (left), at $x = 5000$, and longitudinal (right), at $y = 2500$, profiles of the intensity of the Green function at wavelength 70 with source point $(-5000, 2500)$ and 1000 randomly distributed particles whose parameter $n^2 - 1$ has the value 70.*

3.1. Foldy–Lax formulation.
Let the randomly distributed point scatterers of refractive index n_j be located at $\mathbf{r}_j$, $j = 1, 2, 3, \ldots, J$, and let $G(\mathbf{x}, \mathbf{y}; \omega_l)$ be the Green function. Then the Lippman–Schwinger equation becomes in this case [13]

$$G(\mathbf{x}, \mathbf{y}_n; \omega_l) = G_0(\mathbf{x}, \mathbf{y}_n; \omega_l) + \sum_{j=1}^{J} \tau_j(\omega_l) G_0(\mathbf{x}, \mathbf{r}_j; \omega_l) G(\mathbf{r}_j, \mathbf{y}_n; \omega_l), \quad n = 1, \ldots, N,$$

where the scattering strength τ_j of the jth scatterer is given by

$$(3.1) \qquad\qquad\qquad \tau_j(\omega_l) = \omega_l^2 (n_j^2 - 1) \ell_j^d.$$

Here d is the spatial dimension and ℓ_j is the (linear) size parameter of the jth particle.

The Lippman–Schwinger equation is valid for all $\mathbf{x}$ except at the actual scatterer locations $\mathbf{x} = \mathbf{r}_i$. Thus, to determine $G(\mathbf{r}_j, \mathbf{y}_n; \omega_l)$, we replace the Lippman–Schwinger equation by the Foldy–Lax equation

$$(3.2) \quad G(\mathbf{r}_m, \mathbf{y}_n; \omega_l) = G_0(\mathbf{r}_m, \mathbf{y}_n; \omega_l) + \sum_{j \neq m} \tau_j(\omega_l) G_0(\mathbf{r}_m, \mathbf{r}_j; \omega_l) G(\mathbf{r}_j, \mathbf{y}_n; \omega_l), \quad n = 1, \ldots, N,$$

where the divergent self-field term has been removed. Finding the exciting field $G(\mathbf{r}_j, \mathbf{y}_n; \omega_l)$ is then reduced to inverting a matrix with entries

$$\delta_{ij} - (1 - \delta_{ij}) \tau_j G_0(\mathbf{r}_i, \mathbf{r}_j), \quad i, j = 1, 2, \ldots, J.$$

Once $G(\mathbf{r}_j, \mathbf{y}_n; \omega_l)$ is determined, it is then substituted into the Lippman–Schwinger equation to find the wave field at any location. The numerical scheme is further explicated in Appendix A.

In our simulations, 1000 or 3000 point scatterers are uniformly randomly distributed in the domain $[2000, 4000] \times [0, 5000]$, while the whole computation domain is $[-5000, 5000] \times [0, 5000]$. Some profiles of the Green function are shown in Figure 2.

3.2. Phase-factor of the mean Green function. The full Green function for the cluttered medium, as depicted in Figure 2, is extremely sensitive to the minute displacements of the particles. To improve statistical stability, we use only the averaged quantity of the medium (i.e., the phase of the mean Green function) for imaging.

According to the effective medium theory, the mean transfer function in three spatial dimensions takes the form

$$(3.3) \qquad \bar{H}(\mathbf{x}, \mathbf{y}; \omega) \sim e^{-\frac{r}{2\ell}} \frac{e^{ikr}}{r}, \quad r = |\mathbf{x} - \mathbf{y}|,$$

where the mean-free path ℓ is related to the extinction cross section σ_t by

$$\ell = \frac{1}{\rho \sigma_t},$$

with the particle density ρ. Note that when the particle size a is much greater than the wavelength λ, $\sigma_t \approx 2\pi a^2$, $a =$ radius of particles, and independent of frequency.

On the other hand, when the particle size is much smaller than the wavelength, the extinction cross-section usually depends on the frequency as well. In the case of Rayleigh scattering without absorption, the scattering cross-section scales like ω^{-4},

$$(3.4) \qquad \ell \sim \rho^{-1}(c_0/\omega)^4 a^{-6},$$

where c_0 is the background phase velocity [13]. In the formulation of the phase processor we retain only the travel time part of the mean Green function, corresponding to e^{ikr}.

3.3. Imaging and detection simulations. In the simulations we use $N = 6$ or 11 antennas equally spaced on the side $x = -5000$, $y \in [1500, 3500]$ (total aperture $A = 2000$) and $B = 20$ frequencies corresponding to *equally spaced wavelengths* in the range from 52 to 90. Recall also that the imaging is based on the difference field. Seven targets are located at $[3100, 100]$, $[2800, 1000]$, $[4000, 1600]$, $[3300, 2100]$, $[4500, 3000]$, $[3000, 4000]$, and $[3500, 4800]$. As explained in Appendix A, the numerical scheme is exact within the scope of point scatterers.

In Figure 3 we see that u_R is a more stable imaging function than u itself and that the imaging performance deteriorates as the number of clutter particles increases.

Figure 4 depicts the difference in the stability performance between SA imaging and RM imaging. SA imaging corresponds to having available only the diagonal elements of the RMs and hence is generally less stable, as our stability analysis predicts.

4. Resolution study. The resolutions for one target point in the cluttered medium with 1000 scatterers and in the free-space are shown in Figures 5 and 6, respectively. The transverse and the longitudinal resolutions (vertical axis) are defined as the least distance from the target in the transverse and the longitudinal directions, respectively, where the the imaging function has dropped to half of its maximal value at the target location $(3000, 4000)$. This is called "full width at half maximum" (FWHM), the Houston criterion widely used in astronomy. And for each case we compare the SA resolution to the RM resolution.

Three interesting observations are in order.

(i) The SA resolutions are consistently better than the RM resolutions. The difference is more pronounced in the cross-range resolution than in the range resolution.
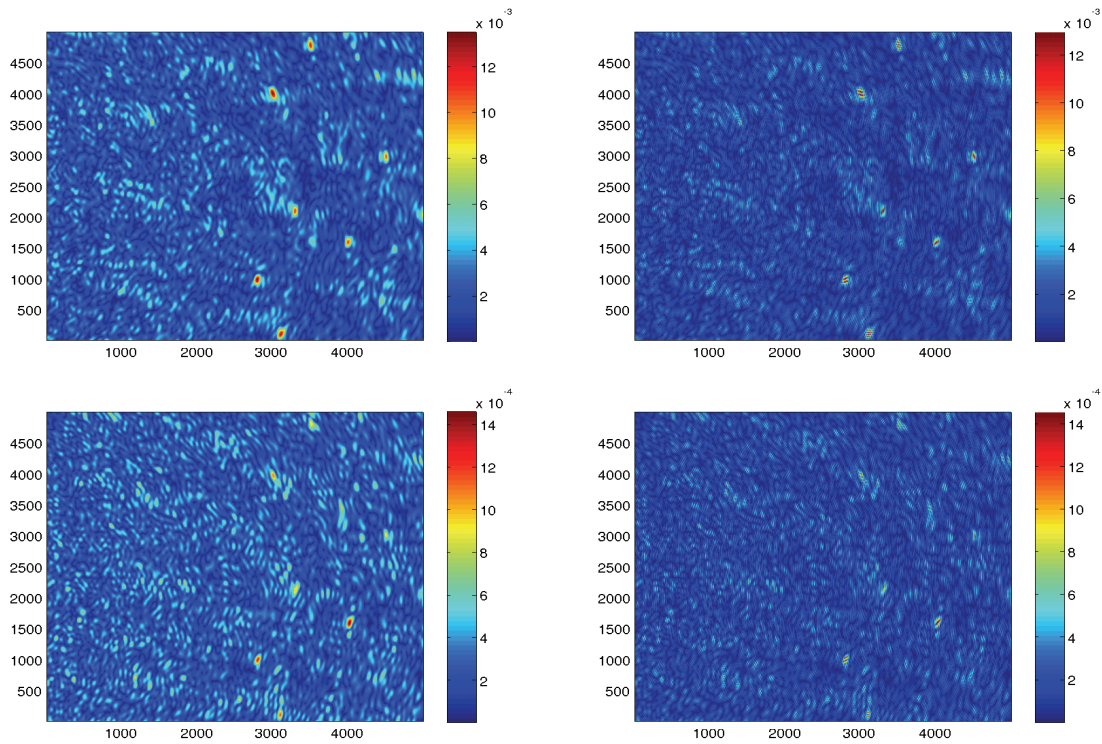
Figure 3. $|u|$ (left column) versus $|u_{\mathrm{R}}|$ (right column) for seven targets with 20 frequencies and 11 antennas (total aperture = 2000) for RM imaging (top row) and SA imaging (bottom row). The values $n^2 - 1$ of the clutter and the targets are 50 and 1, respectively. The top plots are simulated with 1000 particles and the bottom plots with 3000 particles. Note the difference in magnitude between the top and the bottom plots. The plots of $|u_{\mathrm{R}}|$ tend to be more stable than those of $|u|$.
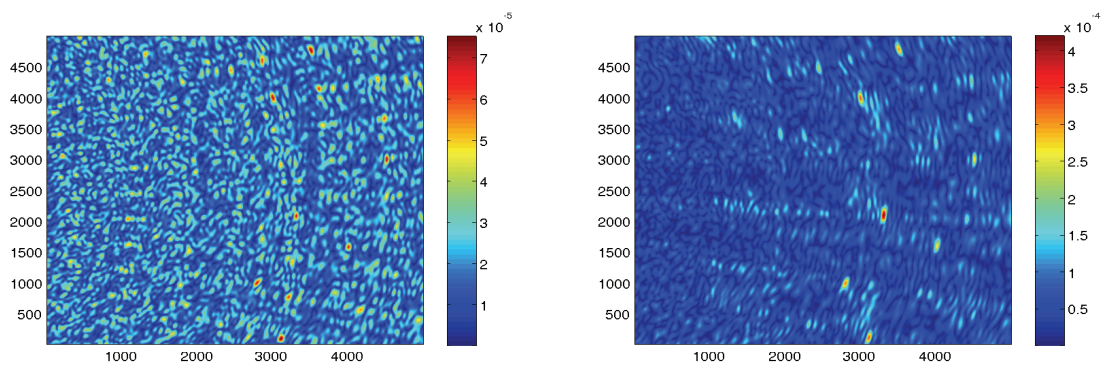

Figure 4. SA (left) and RM (right) images of $|u|$ with seven targets cluttered by 1000 particles and 6 antennas (total aperture = 2000). The values $n^2 - 1$ of the clutter and the targets are 70 and 1, respectively. Note the difference in the magnitude scale between the two plots. The plot on the left is less stable than the plot on the right, as the theory predicts. The SA image is also less stable than the plots on the left column in Figure 3 due to the increase in the clutter strength and the decrease in the antenna number.
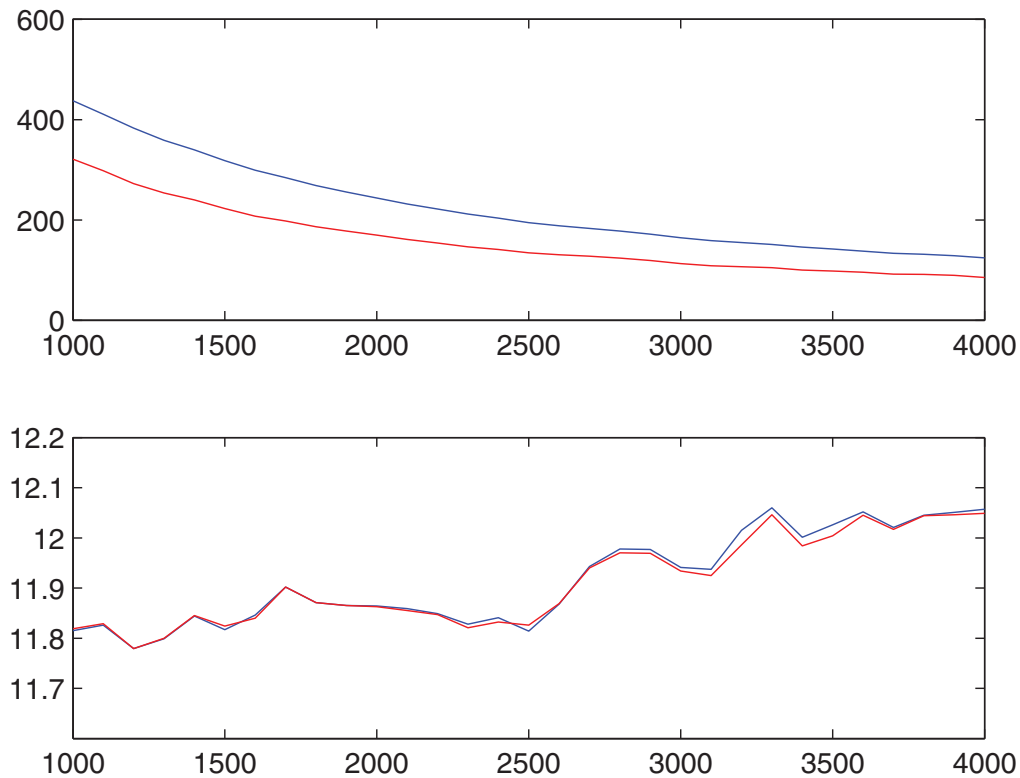
Figure 5. *Comparison of range (bottom) and cross-range (top) resolutions with SA imaging (red) and RM imaging (blue). The values $n^2 - 1$ of the clutter and the target are equal to 50 and 1, respectively. 11 antennas and 1000 particles are used in the simulation. The horizontal axis is the aperture size.*

(ii) The cross-range resolution in both cases decreases with the aperture, consistent with the physical intuition. On the other hand, the range resolution in both cases increases (slowly) with the aperture. In this study, the number of probe positions N is fixed.

(iii) The resolutions have a similar behavior with respect to the change in the antenna/ probe spacing (with A fixed, hence N changing accordingly). Namely, given the same A, the fewer N, the worse the range resolution (in the remote sensing regime) but the better the cross-range resolution; see Figure 7. As N increases, the resolution approaches a finite asymptotic.

Below we give an asymptotic analysis supporting the validity of these counterintuitive effects.

4.1. Cross-range resolution. To simplify the resolution analysis we use the paraxial approximation and consider the two-dimensional case. In the paraxial regime the free-space Green function becomes

$$(4.1) \qquad G_0(x, z) = -\frac{e^{i\pi/4}}{2\sqrt{2\pi}} \frac{e^{ikz}}{\sqrt{kz}} \exp\left[i\frac{kx^2}{2z}\right],$$

where z and x are the longitudinal and transverse coordinates, respectively. In the associated random counterpart called the Markovian model [18], the mean Green function has a similar
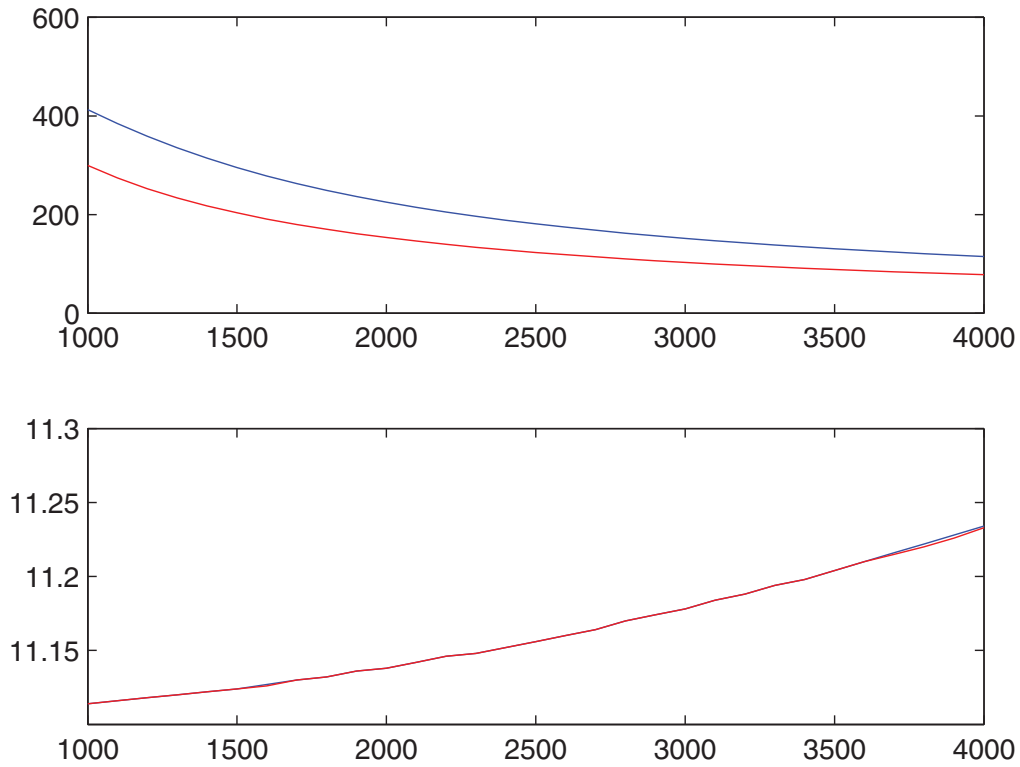
Figure 6. *Resolutions for the free space: The range (bottom) and cross-range (top) resolutions with SA imaging (red) and RM imaging (blue). The horizontal coordinate is the aperture.*
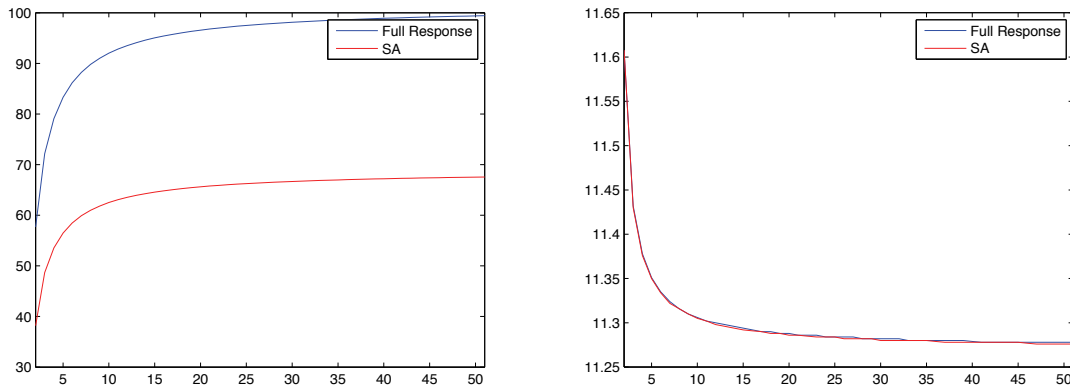

Figure 7. *The cross-range (left) and range (right) resolutions in the free space. The horizontal axis depicts the (integer) number of probe locations. The total aperture is 5000.*

form

$$(4.2) \qquad \bar{G}(x, z) = -\frac{e^{i\pi/4}}{2\sqrt{2\pi}} e^{-k^2 C_0 z} \frac{e^{ikz}}{\sqrt{kz}} \exp\left[i\frac{kx^2}{2z}\right], \quad C_0 > 0,$$

analogous to (3.3). Both (3.3) and (4.2) have the same phase factors as their free-space counterparts. Since we assume the stability regime, the Markovian model and the free-space case yield the similar results. So we will focus on the resolution analysis for one target in the free space. We will neglect the constant factor in (4.1) and (4.2), which does not affect resolution, in the subsequent calculation.

We assume a linear array consisting of N antenna elements equally separated by ℓ_a and located at $(y_j, 0)$ with $y_j = y_1 + (j-1)\ell_a$, $j = 1, \ldots, N$. Let $A = (N-1)\ell_a$ be the total aperture of the array. Without loss of generality, let $y_N = A/2$ and $y_1 = -A/2$. For convenience we assume that B is even and $\omega_i = -\omega_{B+1-i}$ ($i = 1, \ldots, B/2$). We assume that the phase velocity is unity and $\omega = k$.

4.1.1. RM imaging. Let (x_0, z_0) be the location of the target. The RM image u is

$$(4.3) \quad u(x, z) = \sum_{l=1}^{B} \sum_{n,j=1}^{N} |\omega_l|^{-1} z_0^{-1} e^{2i\omega_l(z_0-z)} e^{-i\frac{\omega_l|x-y_n|^2}{2z}} e^{i\frac{\omega_l|x_0-y_n|^2}{2z_0}} e^{-i\frac{\omega_l|x-y_j|^2}{2z}} e^{i\frac{\omega_l|x_0-y_j|^2}{2z_0}}.$$

Note that the image (4.3) is real-valued.

Setting $z = z_0$ and noting that

$$\sum_{n=1}^{N} e^{-i\frac{\omega_l|x-y_n|^2}{2z_0}} e^{i\frac{\omega_l|x_0-y_n|^2}{2z_0}}$$

$$(4.4) \quad = \left[e^{i\ell_a\omega_l(x-x_0)/z_0} - 1 \right]^{-1} e^{-i\frac{\omega_l}{2z_0}(x^2-x_0^2)} \left[e^{-i\frac{\omega_l}{z_0}(x_0-x)\cdot(y_N+\ell_a)} - e^{-i\frac{\omega_l}{z_1}(x_0-x)\cdot y_1} \right],$$

we obtain

$$u(x, z_0) = \sum_{l=1}^{B} |\omega_l|^{-1} z_0^{-1} e^{-i\frac{\omega_l}{z_0}(x^2-x_0^2)}$$

$$\times \left(e^{i\ell_a\omega_l(x-x_0)/z_0} - 1 \right)^{-2} \left(e^{i\frac{\omega_l}{z_0}(x-x_0)\cdot y_{N+1}} - e^{i\frac{\omega_l}{z_0}(x-x_0)\cdot y_1} \right)^2.$$

Here and below, we shall write $y_{N+1} = y_1 + N\ell_a$.

Suppose that $\epsilon \equiv x - x_0$ is so small that the following expansions in the powers of ϵ can be truncated at the second order, namely,

$$e^{-i\frac{\omega_l}{z_0}(x^2-x_0^2)} = 1 - i\frac{\omega_l}{z_0}\epsilon(2x_0 + \epsilon) - \frac{\omega_l^2}{2z_0^2}\epsilon^2(2x_0 + \epsilon)^2 + o(\epsilon^2)$$

$$= 1 - i\epsilon\frac{2\omega_l x_0}{z_0} - \epsilon^2 \left(i\frac{\omega_l}{z_0} + \frac{2\omega_l^2 x_0^2}{z_0^2} \right) + o(\epsilon^2),$$

$$\left(e^{i\ell_a\omega_l(x-x_0)/z_0} - 1 \right)^{-2} = \frac{-z_0^2}{\omega_l^2\ell_a^2\epsilon^2} \left(1 - \frac{i\omega_l\ell_a\epsilon}{z_0} - \frac{5\omega_l^2\ell_a^2\epsilon^2}{12z_0^2} + o(\epsilon^2) \right)$$

and

$$e^{i\frac{\omega_l}{z_0}(x-x_0)\cdot y_{N+1}} - e^{i\frac{\omega_l}{z_0}(x-x_0)\cdot y_1} = i\epsilon N\ell_a\frac{\omega_l}{z_0} \left\{ 1 + \frac{i\omega_l}{2z_0}\epsilon(y_{N+1} + y_1) \right.$$

$$\left. - \frac{\omega_l^2}{6z_0^2}\epsilon^2(y_{N+1}^2 + y_{N+1}y_1 + y_1^2) + o(\epsilon^2) \right\}.$$

Then the imaging function becomes

$$u(x, z_0)$$

$$= \frac{N^2}{z_0} \sum_{l=1}^{B} |\omega_l|^{-1} \left(1 - \frac{i\omega_l \ell_a \epsilon}{z_0} - \frac{5\omega_l^2 \ell_a^2 \epsilon^2}{12 z_0^2}\right) \left(1 - i\epsilon \frac{2\omega_l x_0}{z_0} - \epsilon^2 \left(i\frac{\omega_l}{z_0} + \frac{2\omega_l^2 x_0^2}{z_0^2}\right)\right)$$

(4.5)
$$\times \left(1 + \frac{i\omega_l}{2z_0}\epsilon(y_{N+1} + y_1) - \frac{\omega_l^2}{6z_0^2}\epsilon^2(y_{N+1}^2 + y_{N+1}y_1 + y_1^2)\right)^2 + o(\epsilon^2).$$

Separating (4.5) into terms of different powers of ϵ, we write

(4.6)
$$u(x, z_0) = a_0 + a_1\epsilon + a_2\epsilon^2 + o(\epsilon^2)$$

with

(4.7)
$$a_0 = \frac{N^2}{z_0} \sum_{l=1}^{B} |\omega_l|^{-1},$$

(4.8)
$$a_1 = \frac{iN^2}{z_0^2}(y_N + y_1 - 2x_0) \sum_{l=1}^{B} |\omega_l|^{-1}\omega_l = 0,$$

$$a_2 = \frac{N^2}{z_0} \sum_{l=1}^{B} |\omega_l|^{-1} \left\{-i\frac{\omega_l}{z_0} + \frac{\omega_l^2}{z_0^2}\left(-2x_0^2 + 2x_0(y_{N+1} + y_1)\right.\right.$$

$$\left.\left. - \frac{1}{3}(y_{N+1}^2 + y_{N+1}y_1 + y_1^2) - \frac{1}{4}(y_{N+1} + y_1)^2 - \frac{5}{12}\ell_a^2 + \ell_a(y_{N+1} + y_1 - 2x_0)\right)\right\}$$

(4.9)
$$= -\frac{N^2\epsilon^2}{z_0^3}\left\{\frac{A}{12}(A + 2\ell_a) + 2x_0^2\right\} \sum_{l=1}^{B} |\omega_l| < 0.$$

Conditions (4.8) and (4.9) ensure that the point-target location is the local maximum of the image (4.3) along the cross-range direction.

According to the Houston criterion, the resolution is *inversely* proportional to the square-root of the quantity

(4.10)
$$-\frac{a_2}{a_0} = \frac{\sum_{l=1}^{B} |\omega_l|}{z_0^2 \sum_{l=1}^{B} |\omega_l|^{-1}}\left\{\frac{A}{12}(A + 2\ell_a) + 2x_0^2\right\}.$$

For a target near the imaging axis (i.e., $|x_0| \ll A$) with a densely populated probe location (i.e., $\ell_a \ll A$) and a narrow bandwidth (i.e., $\omega_l \approx \omega$), the classical Rayleigh formula $\sim z_0/(A\omega)$ is recovered.

The other consequence is that for a fixed A the resolution decreases as ℓ_a increases (hence N decreases), resulting in the optimal resolution with $N = 2$.

4.1.2. SA imaging. SA imaging corresponds to having available only the diagonal elements of the response matrices. In this case,

$$u(x,z) = \sum_{l=1}^{B} \sum_{n=1}^{N} |\omega_l|^{-1} z_0^{-1} e^{2i\omega_l(z_0-z)} e^{-i\frac{\omega_l|x-y_n|^2}{z}} e^{i\frac{\omega_l|x_0-y_n|^2}{z_0}}.$$

Following the same calculation as above, we have

$$u(x,z_0)$$

$$= \frac{1}{z_0} \sum_{l=1}^{B} |\omega_l|^{-1} \left(e^{2i\ell_a\omega_l(x-x_0)/z_0} - 1\right)^{-1} e^{-i\frac{\omega_l}{z_0}(x^2-x_0^2)} \left(e^{2i\frac{\omega_l}{z_0}(x-x_0)\cdot y_{N+1}} - e^{2i\frac{\omega_l}{z_0}(x-x_0)\cdot y_1}\right)$$

$$= \frac{N}{z_0} \sum_{l=1}^{B} |\omega_l|^{-1} \left(1 - \frac{i\omega_l \ell_a \epsilon}{z_0} - \frac{\omega_l^2 \ell_a^2 \epsilon^2}{3z_0^2}\right) \left(1 - i\epsilon\frac{2\omega_l x_0}{z_0} - \epsilon^2 \left(i\frac{\omega_l}{z_0} + \frac{2\omega_l^2 x_0^2}{z_0^2}\right)\right)$$

$$\times \left(1 + \frac{i\omega_l}{z_0}\epsilon(y_{N+1} + y_1) - \frac{2\omega_l^2}{3z_0^2}\epsilon^2(y_{N+1}^2 + y_{N+1}y_1 + y_1^2)\right) + o(\epsilon^2)$$

with $\epsilon = x - x_0$. From this the coefficients in the expansion (4.6) can be read:

$$a_0 = \frac{N}{z_0} \sum_{l=1}^{B} |\omega_l|^{-1},$$

(4.11)
$$a_1 = \frac{iN}{z_0^2}(y_N + y_1 - 2x_0) \sum_{l=1}^{B} |\omega_l|^{-1}\omega_l = 0,$$

$$a_2 = \frac{N}{z_0} \sum_{l=1}^{B} |\omega_l|^{-1} \left\{-i\frac{\omega_l}{z_0} + \frac{\omega_l^2}{z_0^2}\left(-2x_0^2 + 2x_0(y_{N+1} + y_1) + \ell_a(y_{N+1} + y_1)\right.\right.$$

$$\left.\left. - \frac{2}{3}(y_{N+1}^2 + y_{N+1}y_1 + y_1^2) - \frac{1}{3}\ell_a^2 - 2\ell_a x_0\right)\right\}$$

(4.12)
$$= -\frac{N\epsilon^2}{z_0^3} \left\{2x_0^2 + \frac{A}{6}(A + 2\ell_a)\right\} \sum_{l=1}^{B} |\omega_l| < 0.$$

Again, conditions (4.11) and (4.12) ensure that the point-target location is the local maximum of the image. The resolution is inversely proportional to the square-root of the following expression:

(4.13)
$$-\frac{a_2}{a_0} = \frac{\sum_{l=1}^{B} |\omega_l|}{z_0^2 \sum_{l=1}^{B} |\omega_l|^{-1}} \left\{2x_0^2 + \frac{A}{6}(A + 2\ell_a)\right\}.$$

For $|x_0|, \ell_a \ll A$, (4.13) predicts a smaller resolution in the case of SA by a factor of $1/\sqrt{2}$ in view of (4.10) and (4.13). As in RM imaging, with a fixed A the resolution decreases as ℓ_a increases (N decreases).

4.2. Range resolution.

4.2.1. RM imaging. Setting $z = z_0$, we have

$$u(x, z_0) = \sum_{l=1}^{B} \sum_{n,j=1}^{N} |\omega_l|^{-1} z_0^{-1} e^{-2i\omega_l \epsilon} e^{i\frac{\omega_l |x_0 - y_n|^2}{2}(-\frac{1}{z} + \frac{1}{z_0})} e^{i\frac{\omega_l |x_0 - y_j|^2}{2}(-\frac{1}{z} + \frac{1}{z_0})},$$

which can be approximated by

$$\frac{1}{\ell_a^2} \sum_{l=1}^{B} |\omega_l|^{-1} z_0^{-1} e^{-2i\omega_l \epsilon} \left(\int_{x_0 - (A+\ell_a)/2}^{x_0 + (A+\ell_a)/2} e^{i\frac{\omega_l |x_0 - y_n|^2}{2}(-\frac{1}{z} + \frac{1}{z_0})} dy_n \right)^2$$

provided that the antennas are so finely spaced that the summation over y_n, y_j can be replaced by an integral.

Calculating up to the second order in ϵ, as before, we have

$$\int_{-(A+\ell_a)/2}^{(A+\ell_a)/2} e^{ix^2 \kappa} dx = \int_{-(A+\ell_a)/2}^{(A+\ell_a)/2} \left(1 + ix^2 \kappa - \frac{1}{2} x^4 \kappa^2 + o(\kappa^2) \right) dx$$

(4.14)
$$= (A + \ell_a) + \frac{1}{12} i (A + \ell_a)^3 \kappa - \frac{1}{160} (A + \ell_a)^5 \kappa^2 + o(\kappa^2)$$

with $\kappa = \frac{\omega_l}{2}(\frac{1}{z_0} - \frac{1}{z})$. Consequently, with $\epsilon = z - z_0$, we have the following expression:

$$u(x, z_0) = \frac{1}{\ell_a^2} \sum_{l=1}^{B} |\omega_l|^{-1} z_0^{-1} e^{-2i\omega_l \epsilon} (A + \ell_a)^2$$

$$\times \left(1 + \frac{i(A+\ell_a)^2}{12} \frac{\omega_l \epsilon}{2z_0(z_0 + \epsilon)} - \frac{(A+\ell_a)^4}{160} \frac{\omega_l^2 \epsilon^2}{4z_0^2(z_0 + \epsilon)^2} + o(\epsilon^2) \right)^2$$

$$= N^2 \sum_{l=1}^{B} |\omega_l|^{-1} z_0^{-1} (1 - 2i\omega_l \epsilon - 2\omega_l^2 \epsilon^2 + o(\epsilon^2)) \left\{ 1 + \frac{i(A+\ell_a)^2 \omega_l \epsilon}{12z_0^2} \right.$$

$$\left. - \frac{(A+\ell_a)^4 \omega_l^2 \epsilon^2}{576 z_0^4} - \frac{i(A+\ell_a)^2 \omega_l \epsilon^2}{12 z_0^3} - \frac{(A+\ell_a)^4 \omega_l^2 \epsilon^2}{320 z_0^4} + o(\epsilon^2) \right\}.$$

The coefficients in the expansion (4.6) are thus given by

(4.15)
$$a_0 = \frac{N^2}{z_0} \sum_{l=1}^{B} |\omega_l|^{-1},$$

(4.16)
$$a_1 = \frac{iN^2}{z_0} \left(-2 + \frac{(A+\ell_a)^2}{12 z_0^2} \right) \sum_{l=1}^{B} |\omega_l|^{-1} \omega_l = 0,$$

$$a_2 = N^2 \sum_{l=1}^{B} |\omega_l|^{-1} z_0^{-1} \left\{ -2\omega_l^2 - \frac{i(A+\ell_a)^2 \omega_l}{12z_0^3} \right.$$

$$\left. + \frac{(A+\ell_a)^2 \omega_l^2}{6z_0^2} - \frac{7(A+\ell_a)^4 \omega_l^2}{1440z_0^4} \right\}$$

(4.17)
$$= -\frac{N^2 \epsilon^2}{z_0} \left\{ 2 - \frac{(A+\ell_a)^2}{6z_0^2} + \frac{7(A+\ell_a)^4}{1440z_0^4} \right\} \sum_{l=1}^{B} |\omega_l| < 0.$$

Equation (4.17) is negative since the propagation distance z_0 is typically larger than the aperture size A in the paraxial regime. The conditions (4.16) and (4.17) ensure that the point-target location is the local maximum of the mean image in the longitudinal direction. The resolution is inversely proportional to the square-root of the following expression:

(4.18)
$$-\frac{a_2}{a_0} = \frac{\sum_{l=1}^{B} |\omega_l|}{\sum_{l=1}^{B} |\omega_l|^{-1}} \left\{ 2 - \frac{(A+\ell_a)^2}{6z_0^2} + \frac{7(A+\ell_a)^4}{1440z_0^4} \right\}.$$

If we completely neglect the second and the third terms in (4.18), then we obtain the longitudinal resolution

$$\sim \left(\frac{\sum_{l=1}^{B} |\omega_l|^{-1}}{\sum_{l=1}^{B} |\omega_l|} \right)^{1/2},$$

which is inversely proportional to the bandwidth, a classical result. When we take into account the perturbative effect of the aperture, the negative sign in the second term in (4.18) implies that the resolution increases with A, as manifest in the bottom plot of Figure 6. Also, in the case of remote sensing $z_0 \gg A$, the second term in (4.18) dominates over the third term. As a result, for a fixed A, the range resolution increases, as ℓ_a increases (N decreases), contrary to the case of cross-range resolution.

4.2.2. SA imaging. As before, we have the following calculation up to the second order in ϵ:

$$\mathbb{E}u(x_0, z) = \sum_{l=1}^{B} \sum_{n=1}^{N} |\omega_l|^{-1} z_0^{-1} e^{-2i\omega_l \epsilon} e^{-i\omega_l |x_0 - y_n|^2 (\frac{1}{z} - \frac{1}{z_0})}$$

$$\approx \frac{1}{\ell_a} \sum_{l=1}^{B} |\omega_l|^{-1} z_0^{-1} e^{-2i\omega_l \epsilon} \int_{x_0 - (A+\ell_a)/2}^{x_0 + (A\ell_a)/2} e^{-i\omega_l |x_0 - y_n|^2 (\frac{1}{z} - \frac{1}{z_0})} dy_n$$

$$= \frac{1}{\ell_a} \sum_{l=1}^{B} \omega_l z_0^{-1} e^{-2i\omega_l \epsilon} (A + \ell_a)$$

$$\times \left(1 + \frac{i(A+\ell_a)^2}{12} \frac{\omega_l \epsilon}{z_0(z_0 + \epsilon)} - \frac{(A+\ell_a)^4}{160} \frac{\omega_l^2 \epsilon^2}{z_0^2 (z_0 + \epsilon)^2} + o(\epsilon^2) \right)$$

$$= N \sum_{l=1}^{B} |\omega_l|^{-1} z_0^{-1} (1 - 2i\omega_l \epsilon - 2\omega_l^2 \epsilon^2 + o(\epsilon^2))$$

$$\times \left(1 + \frac{i\omega_l (A+\ell_a)^2}{12z_0^2} \epsilon - \frac{i\omega_l (A+\ell_a)^2}{12z_0^3} \epsilon^2 - \frac{\omega_l^2 (A+\ell_a)^4}{160z_0^4} \epsilon^2 + o(\epsilon^2) \right).$$

Hence the coefficients in the expansion (4.6) are

$$(4.19) \qquad a_0 = \frac{N}{z_0} \sum_{l=1}^{B} |\omega_l|^{-1},$$

$$(4.20) \qquad a_1 = \frac{iN}{z_0} \left(-2 + \frac{(A + \ell_a)^2}{12z_0^2} \right) \sum_{l=1}^{B} |\omega_l|^{-1} \omega_l = 0,$$

$$(4.21) \qquad a_2 = -\frac{N}{z_0} \left(2 - \frac{(A + \ell_a)^2}{6z_0^2} + \frac{(A + \ell_a)^4}{160z_0^4} \right) \sum_{l=1}^{B} |\omega_l| < 0.$$

The conditions (4.20) and (4.21) ensure that the point-target location is the local maximum of the image along the range direction. The resolution is inversely proportional to the square-root of the following quantity:

$$(4.22) \qquad -\frac{a_2}{a_0} = \frac{\sum_{l=1}^{B} |\omega_l|}{\sum_{l=1}^{B} |\omega_l|^{-1}} \left\{ 2 - \frac{(A + \ell_a)^2}{6z_0^2} + \frac{(A + \ell_a)^4}{160z_0^4} \right\}.$$

Comparing (4.22) with (4.18), we see that the difference is in the third terms of the respective expressions, resulting in a slightly better resolution for SA imaging. Again, in the case of remote sensing $z_0 \gg A$ with a fixed A, the range resolution increases with ℓ_a.

5. Statistical detection. In this section, we consider the regime where the stability condition is not satisfied and the raw image is noisy due to interference from clutter and other targets (see the left plot in Figure 9). This calls for a statistical detection scheme. To this end, it is advantageous to work with the more stable imaging function u_R instead of u.

Under the Gaussian assumption, $u_\mathrm{R}(\mathbf{r})$ has a χ^2-type distribution for each $\mathbf{x}$. To simplify the discussion we neglect the quadratic-in-h terms. This can be justified when, e.g., $K \gg 1$; see Appendix C. Then (2.5) becomes

$$(5.1) \qquad u_\mathrm{R}(\mathbf{x}) = \Re \left\{ \sum_{l=1}^{B} \sum_{i=1}^{M} \sum_{j=1}^{N} \tau_i(\omega_l) P(\mathbf{x}, \mathbf{y}_j; \omega_l) \big(\bar{H}_{ij}^2(\omega_l) + 2\bar{H}_{ij}(\omega_l) h_{ij}(\omega_l) \big) P(\mathbf{y}_j, \mathbf{x}; \omega_l) \right\},$$

which has the Gaussian distribution of the mean and variance:

$$(5.2) \qquad \mathbb{E}(u_\mathrm{R}(\mathbf{x})) = \Re \left\{ \sum_{l=1}^{B} \sum_{i=1}^{M} \sum_{j=1}^{N} \tau_i(\omega_l) P(\mathbf{x}, \mathbf{y}_j; \omega_l) \bar{H}_{ij}^2(\omega_l) P(\mathbf{y}_j, \mathbf{x}; \omega_l) \right\},$$

$$\mathrm{Var}(u_\mathrm{R}(\mathbf{x})) = 2\eta^2 \sum_{l=1}^{B} \sum_{i=1}^{M} \sum_{j=1}^{N} |\tau_i(\omega_l)|^2 |P(\mathbf{x}, \mathbf{y}_j; \omega_l)|^2 |P(\mathbf{y}_j, \mathbf{x}; \omega_l)|^2 |\bar{H}_{ij}(\omega_l)|^2$$

$$(5.3) \qquad = 2\eta^2 \sum_{l=1}^{B} \sum_{i=1}^{M} \sum_{j=1}^{N} |\tau_i(\omega_l)|^2 |\bar{H}_{ij}(\omega_l)|^2.$$

Here we have used the fact that $|P(\mathbf{x}, \mathbf{y}; \omega)| = 1$ since the back-propagator P is chosen to be the *conjugate* phase factor of the mean Green function. For simplicity, we consider the case of identical point targets $\tau_i = \tau$, $i = 1, \ldots, M$.

For each point $\mathbf{x}$ in the search domain, we postulate the following alternatives:

$$\begin{cases} \mathcal{H}_0(\mathbf{x}): & \mathbf{x} \text{ is far away from all targets,} \\ \mathcal{H}_1(\mathbf{x}): & \mathbf{x} \text{ is close to any target.} \end{cases}$$

By the assumption of widely separated targets, $\mathbb{E}u_{\mathrm{R}}$ under hypothesis $\mathcal{H}_0$ should be approximately zero, while under $\mathcal{H}_1$ it can be approximated by

$$(5.4) \qquad \nu(\mathbf{x}) = \sum_{l=1}^{B} \sum_{j=1}^{N} \tau(\omega_l) |\bar{H}(\mathbf{x}, \mathbf{y}_j; \omega_l)|^2,$$

since one particular target will dominate the summation over i in (5.2). $\nu(\mathbf{x})$ can be calculated with the knowledge of τ and $\bar{H}$. On the other hand, the variance under either hypothesis is the same as

$$\sigma^2 = 2\eta^2 \sum_{l=1}^{B} \sum_{i=1}^{M} \sum_{j=1}^{N} |\tau(\omega_l)|^2 |\bar{H}_{ij}(\omega_l)|^2,$$

which is independent of the test point $\mathbf{x}$ but dependent on the locations of the targets.

In the numerical experiment below, we make the approximation $|\bar{H}_{ij}(\omega_l)| \approx \mu(\omega_l)$ assuming that the targets are roughly the same distance from the array and estimate σ^2 to be

$$(5.5) \qquad \sigma^2 \approx 2\eta^2 MN \sum_{l}^{B} |\tau(\omega_l)|^2 \mu(\omega_l),$$

provided that M is known.

The Neyman–Pearson lemma states that when choosing between $\mathcal{H}_0$ and $\mathcal{H}_1$ with a prescribed false alarm rate α, the likelihood ratio test that rejects $\mathcal{H}_0$ in favor of $\mathcal{H}_1$ if the corresponding likelihood is above a threshold (e^γ) is the most powerful test. The threshold is determined by

$$(5.6) \qquad \frac{\text{p.d.f. of } u_{\mathrm{R}}(\mathbf{x})|_{\mathcal{H}_1}}{\text{p.d.f. of } u_{\mathrm{R}}(\mathbf{x})|_{\mathcal{H}_0}} = e^{-\frac{1}{2\sigma^2}(u_{\mathrm{R}} - \nu)^2} / e^{-\frac{1}{2\sigma^2} u_{\mathrm{R}}^2} = e^{-\frac{1}{2\sigma^2}(-2u_{\mathrm{R}}\nu + \nu^2)} > e^\gamma,$$

which implies

$$(5.7) \qquad \frac{u_{\mathrm{R}}}{\sigma} > \frac{\gamma \sigma}{\nu} + \frac{\nu}{2\sigma}.$$

Under the hypothesis $\mathcal{H}_0$,

$$Y_0 \equiv \frac{u_{\mathrm{R}}}{\sigma} \sim N(0, 1).$$

Consequently, for the false alarm rate α we have

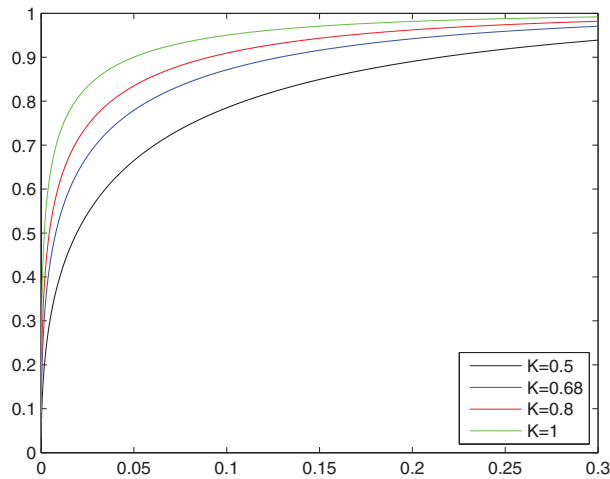$$\frac{\gamma \sigma}{\nu} + \frac{\nu}{2\sigma} = Q^{-1}(1 - \alpha),$$

Figure 8. *ROC curves with $B = 20$ frequencies, $N = 6$ antennas, and $M = 7$ targets at various K's.*

where Q is the standard *cumulative* Gaussian probability function. Hence

$$(5.8) \qquad \gamma = \frac{\nu}{\sigma} Q^{-1}(1 - \alpha) - \frac{\nu^2}{2\sigma^2}.$$

On the other hand, under the hypothesis $\mathcal{H}_1$,

$$Y_1 \equiv \frac{u_{\mathrm{R}} - \nu}{\sigma} \sim N(0, 1),$$

and the detection rule (5.7) gives rise to a miss probability β satisfying

$$(5.9) \qquad \frac{\gamma\sigma}{\nu} - \frac{\nu}{2\sigma} = Q^{-1}(\beta).$$

By (5.8) and (5.9), we obtain the detection rate $P_d \equiv 1 - \beta$ as a function of α:

$$(5.10) \qquad P_d = 1 - Q\left(Q^{-1}(1 - \alpha) - \frac{\nu}{\sigma}\right).$$

The graphs of P_d as a function of α are called the receiver operating characteristic (ROC) curves which are parametrized by $\nu(\mathbf{x})/\sigma$.

The ROC curves are shown in Figure 8 with $B = 20$, $N = 6$, $M = 7$, and different K's. For these parameters, the quadratic-in-h terms in the imaging function begin to have a smaller magnitude than the linear-in-h terms when $K > 1/2$. Although the curves are determined by ν/σ only, they may vary with the search point $\mathbf{x}$ since the Rician factor K is a function of the location $\mathbf{x}$ in general.

The above scheme can be easily extended to the case of RM imaging. The main difference is in the evaluation of $\mathbb{E}u_{\mathrm{R}}$ and $\mathrm{Var}(u_{\mathrm{R}})$ in (5.2)–(5.3). We leave it to the reader to work this out. Despite the crude approximations assumed in the scheme, the imaging performance is good with a suitably chosen false alarm rate that produces exactly M positive detections, where M is the number of target points (Figure 9).
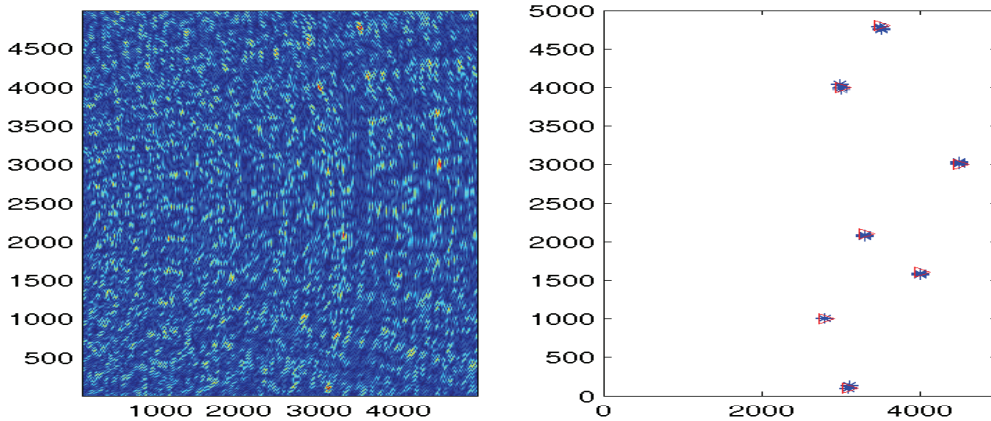
Figure 9. *SA image $|u_{\mathrm{R}}|$ (left) and statistical detection figure (right) of 7 targets with 6 transducers and 20 frequencies. The number of clutter scatterers is 1000. The values $n^2 - 1$ of the clutter and the targets are 70 and 1, respectively. The false-alarm-rate α of the detection algorithm is 0.15%. The red triangles denote the true targets' locations, and the blue stars are the results of the detection. When α is low, it is possible to miss some of the targets, and when α is high, false target image may show up.*

6. Conclusions. We have revisited the problem of imaging a set of point targets based on the scattered wave field at a number of discrete frequencies as recorded by an antenna array. The target scatterers are masked by a large number of "clutter" particles. We have derived the stability condition for the SA imaging array and compared it with that for RM imaging previously obtained in [10]. Not surprisingly, SA imaging is typically less stable than RM imaging, which has a larger degree of freedom in the measurement resources for the same N and B.

Our resolution analysis of SA imaging and RM imaging has revealed several counterintuitive effects: First, given the same measurement resources (N, B), SA imaging has better resolution performance, although less stable, than RM imaging; second, for both imaging methods, the cross-range resolution as measured by FWHM decreases with the aperture and the antenna/probe spacing while the range resolution increases (slightly) with the two parameters.

Finally, for the noisy, unstable regime we have tentatively proposed a detection scheme for deciding if a target is present at a particular location, which optimally adapts to the clutter present in the scenery at hand. With the knowledge of the total number M of targets the detection scheme has a surprisingly good performance despite the crude approximations assumed in the scheme.

Appendix A. Stability analysis. In this section we derive for the Rician channels the stability condition (1.1). Under this stability condition the image $u(\mathbf{x})$ (respectively, $u_{\mathrm{R}}(\mathbf{r})$) is approximately equal to its mean $\mathbb{E}u(\mathbf{x})$ (respectively, $\mathbb{E}u_{\mathrm{R}}(\mathbf{x})$). For the sake of notational simplicity, the stability analysis below is carried out for u.

Observe first that the expectation for u is given by

$$\mathbb{E}u(\mathbf{x}) = \sum_{l=1}^{B}\sum_{i=1}^{M}\sum_{n=1}^{N} \tau_i(\omega_l) P(\mathbf{x}, \mathbf{y}_n; \omega_l)\left(\bar{H}_{in}^2(\omega_l) + \mathbb{E}\left[h_{in}^2(\omega_l)\right]\right) P(\mathbf{y}_n, \mathbf{x}; \omega_l)$$

$$\approx \sum_{l=1}^{B}\sum_{i=1}^{M}\sum_{n=1}^{N}\tau_i(\omega_l)P(\mathbf{x},\mathbf{y}_n;\omega_l)\bar{H}_{in}^2(\omega_l)P(\mathbf{y}_n,\mathbf{x};\omega_l)$$

$$\text{(A.1)} \qquad = O(|\tau|\mu^2 BN).$$

The apparent missing of a factor M in the above estimate is due to the choice of P as the conjugate phase-factor of the mean Green function. As a result the leading contribution is from the few targets closest to the point $\mathbf{x}$, and thus there are effectively $O(1)$ terms in the above summation over i [10].

Note also that the expression for u contains a *product* of elements of $\mathbf{H}$. As a result, the expectation of u involves the second order moments of h, and the variance of u involves the fourth order moments of h. In calculation of the fourth order moments we shall use the assumption of Gaussian statistics. The Gaussian assumption is widely used and includes the Rician and Rayleigh fading channels in wireless modeling [4, 16].

Using the Gaussian moment assumption, we obtain

$$\mathbb{E}|u(\mathbf{x})|^2 \approx \left|\sum_{l=1}^{B}\sum_{i=1}^{M}\sum_{n=1}^{N}\tau_i(\omega_l)P(\mathbf{x},\mathbf{y}_n;\omega_l)\bar{H}_{in}^2(\omega_l)P(\mathbf{y}_n,\mathbf{x};\omega_l)\right|^2$$

$$+ 4\mathbb{E}\left\{\left|\sum_{l=1}^{B}\sum_{i=1}^{M}\sum_{n=1}^{N}\tau_i(\omega_l)P(\mathbf{x},\mathbf{y}_n;\omega_l)\bar{H}_{in}h_{in}(\omega_l)P(\mathbf{y}_n,\mathbf{x};\omega_l)\right|^2\right\}$$

$$\text{(A.2)} \qquad + \mathbb{E}\left\{\left|\sum_{l=1}^{B}\sum_{i=1}^{M}\sum_{n=1}^{N}\tau_i(\omega_l)P(\mathbf{x},\mathbf{y}_n;\omega_l)h_{in}^2(\omega_l)P(\mathbf{y}_n,\mathbf{x};\omega_l)\right|^2\right\},$$

which becomes after using (2.2)

$$\mathbb{E}|u(\mathbf{x})|^2 \approx \left|\mathbb{E}u(\mathbf{x})\right|^2 + 2\eta^2\sum_{l=1}^{B}\sum_{i=1}^{M}\sum_{n=1}^{N}|\tau_i(\omega_l)|^2\left|P(\mathbf{x},\mathbf{y}_n;\omega_l)\right|^2|\bar{H}_{in}|^2|P(\mathbf{y}_n,\mathbf{x};\omega_l)|^2$$

$$+ 2\eta^2\sum_{l=1}^{B}\sum_{i=1}^{M}\sum_{n=1}^{N}|\tau_i(\omega_l)|^2|P(\mathbf{x},\mathbf{y}_n;\omega_l)|^2|\bar{H}_{in}(\omega_l)|^2|P(\mathbf{y}_n,\mathbf{x};\omega_l)|^2$$

$$+ 2\eta^4\sum_{l=1}^{B}\sum_{i=1}^{M}|\tau_i(\omega_l)|^2\sum_{n=1}^{N}\left|P(\mathbf{x},\mathbf{y}_n;\omega_l)\right|^2\left|P(\mathbf{y}_n,\mathbf{x};\omega_l)\right|^2$$

$$\text{(A.3)} \qquad = \left|\mathbb{E}u(\mathbf{x})\right|^2 + O|\tau|^2\eta^2(\mu^2 BMN + \eta^2 BMN) \quad \text{as } B, N \to \infty.$$

Therefore, for an active array, we have $\mathfrak{R} \gg 1$ when (1.1) holds.

Appendix B. The Foldy–Lax formulation. Let $\mathbf{x}_m$, $m = 1,\dots,M$, be the locations of the M target points and $\mathbf{x}_{M+j}$, $j = 1,\dots,J$, the locations of the J clutter points. The total Green function $G_T(\mathbf{r},\mathbf{y}_i;\omega)$ in the presence of both clutter and target particles satisfies

$$\text{(B.1)} \qquad G_T(\mathbf{r},\mathbf{y}_i;\omega) = G_0(\mathbf{r},\mathbf{y}_i;\omega) + \sum_{m=1}^{M+J}\tau(\mathbf{x}_m,\omega)G_0(\mathbf{r},\mathbf{x}_m;\omega)G_T(\mathbf{x}_m,\mathbf{y}_i;\omega).$$

The scattering amplitude function at scatterer m is $\tau_m = \tau(\mathbf{x}_m, \omega)$. Evaluation at the scatterers then gives the Foldy–Lax equations:

$$G_T(\mathbf{x}_j, \mathbf{y}_i; \omega) = G_0(\mathbf{x}_j, \mathbf{y}_i; \omega) + \sum_{m \neq j} \tau_m G_0(\mathbf{x}_j, \mathbf{x}_m; \omega) G_T(\mathbf{x}_m, \mathbf{y}_i; \omega), \quad j = 1, \ldots, M + J.$$

Consequently, the exciting field at the target locations is determined by

(B.2)
$$\begin{pmatrix} G_T(\mathbf{x}_1, \mathbf{y}_i; \omega) \\ G_T(\mathbf{x}_2, \mathbf{y}_i; \omega) \\ \vdots \\ G_T(\mathbf{x}_{M+J}, \mathbf{y}_i; \omega) \end{pmatrix} = \mathbf{F}_\omega^{-1} \begin{pmatrix} G_0(\mathbf{x}_1, \mathbf{y}_i; \omega) \\ G_0(\mathbf{x}_2, \mathbf{y}_i; \omega) \\ \vdots \\ G_0(\mathbf{x}_{M+J}, \mathbf{y}_i; \omega) \end{pmatrix},$$

where

$$\mathbf{F}_\omega = \begin{pmatrix} 1 & -\tau_2 G_0(\mathbf{x}_1, \mathbf{x}_2; \omega) & \ldots & -\tau_{M+J} G_0(\mathbf{x}_1, \mathbf{x}_{M+J}; \omega) \\ -\tau_1 G_0(\mathbf{x}_2, \mathbf{x}_1; \omega) & 1 & \ldots & -\tau_{M+J} G_0(\mathbf{x}_2, \mathbf{x}_{M+J}; \omega) \\ \ldots & \ldots & \ddots & \ldots \\ -\tau_1 G_0(\mathbf{x}_{M+J}, \mathbf{x}_1; \omega) & -\tau_2 G_0(\mathbf{x}_{M+J}, \mathbf{x}_2; \omega) & \ldots & 1 \end{pmatrix}.$$

The vector on the left-hand side of (B.2) in turn determines the scattered field through (B.1).

For $m = 1, \ldots, M + J$, define the vector $\vec{G}_0(\mathbf{x}_m)$ as

$$\vec{G}_0(\mathbf{x}_m, \omega) = (G_0(\mathbf{x}_m, \mathbf{y}_1; \omega), G_0(\mathbf{x}_m, \mathbf{y}_2; \omega), \ldots, G_0(\mathbf{x}_m, \mathbf{y}_N; \omega))^t,$$

where t denotes the matrix transpose. The full response matrix $\mathbf{R}$ is an $N \times N$ square matrix given by

$$\mathbf{R}(\omega) = \begin{pmatrix} \tau_1 \vec{G}_0(\mathbf{x}_1, \omega) & \tau_2 \vec{G}_0(\mathbf{x}_2, \omega) & \ldots & \tau_{M+J} \vec{G}_0(\mathbf{x}_{M+J}, \omega) \end{pmatrix} \mathbf{F}_\omega^{-1} \begin{pmatrix} \vec{G}_0^t(\mathbf{x}_1, \omega) \\ \vec{G}_0^t(\mathbf{x}_2, \omega) \\ \vdots \\ \vec{G}_0^t(\mathbf{x}_{M+J}, \omega) \end{pmatrix}.$$

Similarly, we can simulate the wave fields in the presence of clutter particles only. Note that in the Foldy–Lax simulation, we do not make the DWBA assumption.

Appendix C. Simplified imaging function. We show that under the condition $K \gg 1$ the quadratic-in-h term in (2.5) is negligible. First we write explicitly

$$u_R(\mathbf{x}) = \Re \left\{ \sum_{l=1}^B \sum_{i=1}^M \sum_{j=1}^N \tau_i(\omega_l) P(\mathbf{x}, \mathbf{y}_j; \omega_l) H_{ij}^2(\omega_l) P(\mathbf{y}_j, \mathbf{x}; \omega_l) \right\}$$

(C.1)
$$= \Re \left\{ \sum_{l=1}^B \sum_{i=1}^M \sum_{j=1}^N \tau_i(\omega_l) P(\mathbf{x}, \mathbf{y}_j; \omega_l) \bar{H}_{ij}^2(\omega_l) P(\mathbf{y}_j, \mathbf{x}; \omega_l) \right\}$$

(C.2)
$$+ \Re \left\{ \sum_{l=1}^B \sum_{i=1}^M \sum_{j=1}^N \tau_i(\omega_l) P(\mathbf{x}, \mathbf{y}_j; \omega_l) 2 \bar{H}_{ij}(\omega_l) h_{ij}(\omega_l) P(\mathbf{y}_j, \mathbf{x}; \omega_l) \right\}$$

(C.3)
$$+ \Re \left\{ \sum_{l=1}^B \sum_{i=1}^M \sum_{j=1}^N \tau_i(\omega_l) P(\mathbf{x}, \mathbf{y}_j; \omega_l) h_{ij}^2(\omega_l) P(\mathbf{y}_j, \mathbf{x}; \omega_l) \right\}.$$

The (C.1) term is a deterministic term, while the (C.2) and (C.3) terms are random with mean zero. We show next that the variance of (C.2) is larger than that of (C.3) in the case $K \gg 1$.

The variance of (C.2) is

$$2\eta^2 \sum_{l=1}^{B} \sum_{i=1}^{M} \sum_{j=1}^{N} |\tau_i(\omega_l)|^2 |P(\mathbf{x}, \mathbf{y}_j; \omega_l)|^2 |P(\mathbf{y}_j, \mathbf{x}; \omega_l)|^2 |\bar{H}_{ij}(\omega_l)|^2$$

$$= 2\eta^2 \sum_{l=1}^{B} \sum_{i=1}^{M} \sum_{j=1}^{N} |\tau_i(\omega_l)|^2 |\bar{H}_{ij}(\omega_l)|^2$$

$$\approx 2\mu^2 \eta^2 BMN |\tau|^2,$$

and the variance of (C.3) is

$$\eta^4 \sum_{l=1}^{B} \sum_{i=1}^{M} \sum_{j=1}^{N} |\tau_i(\omega_l)|^2 |P(\mathbf{x}, \mathbf{y}_j; \omega_l)|^2 |P(\mathbf{y}_j, \mathbf{x}; \omega_l)|^2$$

$$= \eta^4 \sum_{l=1}^{B} \sum_{i=1}^{M} \sum_{j=1}^{N} |\tau_i(\omega_l)|^2$$

$$\approx \eta^4 BMN |\tau|^2.$$

The ratio of the former to the latter is proportional to $K \gg 1$.

REFERENCES

[1] A. B. BAGGEROER, W. A. KUPERMAN, AND P. N. MIKHALEVSKY, *An overview of matched field methods in ocean acoustics*, IEEE J. Oceanic Eng., 18 (1993), pp. 401–424.

[2] M. CHENEY, *A mathematical tutorial on synthetic aperture radar*, SIAM Rev., 43 (2001), pp. 301–312.

[3] A. J. DEN DEKKER AND A. VAN DEN BOS, *Resolution: A survey*, J. Opt. Soc. Amer. A, 14 (1997), pp. 547–557.

[4] G. D. DURGIN, *Space-Time Wireless Channels*, Prentice–Hall, Englewood Cliffs, NJ, 2003.

[5] A. FANNJIANG, *Time reversal communication in Rayleigh fading broadcast channels with pinholes*, Phys. Lett. A, 353 (2006), pp. 389–397.

[6] A. FANNJIANG, *Information transfer in disordered media by broadband time reversal: Stability, resolution and capacity*, Nonlinearity, 19 (2006), pp. 2425–2439.

[7] A. FANNJIANG, *On Time Reversal Mirrors*, http://arxiv.org/abs/0811.0132.

[8] A. FANNJIANG AND K. SOLNA, *Superresolution and duality for time-reversal of waves in random media*, Phys. Lett. A, 352 (2005), pp. 22–29.

[9] A. FANNJIANG AND K. SOLNA, *Broadband resolution analysis for imaging with measurement noise*, J. Opt. Soc. Amer. A, 24 (2007), pp. 1623–1632.

[10] A. FANNJIANG AND P. YAN, *Multi-frequency imaging of multiple targets in Rician fading channels: Stability and resolution*, Inverse Problems, 23 (2007), pp. 1801–1819.

[11] L. L. FOLDY, *The multiple scattering of waves*, Phys. Rev., 67 (1945), pp. 107–119.

[12] B. R. FRIEDEN, *On arbitrarily perfect imagery with a finite aperture*, Opt. Acta, 16 (1969), pp. 795–807.

[13] A. ISHIMARU, *Wave Propagation and Scattering in Random Media*, Vols. 1 and 2, Academic Press, New York, 1978.

[14] M. LAX, *Multiple scattering of waves*, Rev. Modern Phys., 23 (1951), pp. 287–310.

[15] M. Lax, *Multiple scattering of waves* II. *The effective field in dense systems*, Phys. Rev., 85 (1952), pp. 261-269.

[16] J. G. Proakis, *Digital Communications*, 4th ed., McGraw-Hill, New York, 2001.

[17] M. Shahram and P. Milanfar, *Imaging below the diffraction limit: A statistical analysis*, IEEE Trans. Image Process., 13 (2004), pp. 677–689.

[18] J. W. Strohbehn, *Laser Beam Propagation in the Atmosphere*, Springer-Verlag, Berlin, 1978.

[19] A. Tolstoy, *Matched Field Processing in Underwater Acoustics*, World Scientific, Singapore, 1993.

[20] G. Toraldo di Francia, *Resolving power and information*, J. Opt. Soc. Amer., 45 (1955), pp. 497–501.

[21] S van Aert, D. van Dyck, and A. J. den Dekker, *Resolution of coherent and incoherent imaging systems reconsidered: Classical criteria and a statistical alternative*, Opt. Express, 14 (2006), pp. 3830–3839.

[22] H. C. Van der Hulst, *Light Scattering by Small Particles*, Dover, New York, 1981.

[23] N. J. Vershad, *Resolution, optical-channel capacity and information theory*, J. Opt. Soc. Amer., 59 (1969), pp. 157–163.

[24] B. Yazici, M. Cheney, and C. E. Yarman, *Synthetic-aperture inversion in the presence of noise and clutter*, Inverse Problems, 22 (2006), pp. 1705–1729.